

Polarization Diversity-enabled LOS/NLOS Identification via Carrier Phase Measurements

Onel L. A. López, *Member, IEEE*, Dileep Kumar, *Student Member, IEEE*, and Antti Tölli, *Senior Member, IEEE*

Abstract

Provision of accurate localization is an increasingly important feature of wireless networks. To this end, reliable distinction between line-of-sight (LOS) and non-LOS (NLOS) radio links is necessary to avoid degenerative localization estimation biases. Interestingly, LOS and NLOS transmissions affect differently the polarization of receive signals. In this work, we leverage this phenomenon to propose a threshold-based LOS/NLOS classifier exploiting weighted differential carrier phase measurements over a single link with different polarization configurations. Operation in full and limited polarization diversity systems are both possible. We develop a framework for assessing the performance of the proposed classifier, and show through simulations the performance impact of the reflecting materials in NLOS scenarios. For instance, the classifier is far more efficient in NLOS scenarios with wooden reflectors than in those with metallic reflectors. Numerical results evince the potential performance gains from exploiting full polarization diversity, properly weighting the differential carrier phase measurements, and using multi-signal/tone transmissions. Finally, we show that the optimum decision threshold is inversely proportional to the path power gain in dB, while it does not depend significantly on the material of potential NLOS reflectors.

Index Terms

LOS/NLOS detection, polarization, phase measurements, localization

I. INTRODUCTION

Accurate localization (positioning) is a key feature/service of the fifth generation (5G) and beyond wireless networks [1]. Applications are numerous, including enhanced emergency call

Authors are with the Centre for Wireless Communications, University of Oulu, Finland, e-mails: {Onel.AlcarazLopez, Dileep.Kumar, Antti.Tolli}@oulu.fi

This research has been supported by the Academy of Finland, 6G Flagship program under Grant 346208.

localization, personal navigation, robot/drone/vehicle tracking, autonomous driving, and social networking. Location side-information can also serve, for example, to predict received power levels (including experienced interference) and channel state information (CSI), as a node/beam association criterion, and to enable efficient relay selection and routing strategies, thus facilitating optimized communication network design and operation [2]–[5].

The 3rd Generation Partnership Project (3GPP) is in charge of defining cellular connectivity standards. 3GPP Rel-15 [6] is the first release of the 5G standard, while specifications related to cellular-based positioning were first defined in 3GPP Rel-16 [7]. Later on, meter and sub-meter positioning accuracy targets were set in 3GPP Rel-17 [8], [9] (e.g., 0.2 m and 1 m positioning accuracy in horizontal and vertical dimension respectively for 90% of the users in Industrial Internet of Things (IIoT) use cases). To support such stringent requirements, operation at millimeter (mm)-wave and terahertz bands, together with the exploitation of large bandwidths and highly directional transmissions from massive antenna arrays, are usually required since they inherently provide higher temporal, spatial, and angular resolutions [8]–[11]. These techniques and operation regimes are leveraged by radio access technology (RAT)-dependent positioning solutions, such as Time-of-Arrival (ToA), Time-Difference-of-Arrival (TDoA), Multi-Cell Round-Trip-Time (Multi-RTT), Angle-of-Departure (AoD), Angle-of-Arrival (AoA), and Enhanced Cell ID (E-CID), supported by 5G, in addition to RAT-independent solutions relying on Global Navigation Satellite System (GNSS), barometric pressure, and other techniques [12]. However, the current positioning methods alone cannot meet the aforementioned requirements, as shown by the evaluation results in [13]–[15]. Thus, to support sub-meter level accuracy, it was recently agreed to consider the carrier-phase based ranging as one of the candidates for the study of RAT-dependent high-accuracy positioning [16]–[18].

A. The LOS/NLOS Identification Problem

Traditionally, scattering or multi-path propagation has been considered a critical problem for attaining accurate positioning. Consequently, multi-path mitigation techniques have been continuously developed to combat its detrimental effect. More recently, multi-path exploitation mechanisms, where scattered and reflected signals are not seen as a disturbance but as a source of additional information [19], [20], are also proposed for greater performance enhancements. In either case, one problem that persists lies in determining whether transmitter and receiver are, or are not, under line-of-sight (LOS). Note that in many environments there may be obstacles

blocking the LOS connection between the nodes (i.e., non-LOS (NLOS) situation), thereby potentially introducing biases in the distance estimation. Therefore, distinguishing NLOS from LOS channels is critical for attaining accurate positioning estimates, and constitutes the focus of our work.

B. State of the Art on LOS/NLOS Identification

In recent years, the LOS/NLOS identification problem has received significant attention. Basically, LOS/NLOS classifiers are based on *i*) thresholding, where a relevant (or combination of relevant) statistic(s) is compared to a given threshold to infer a decision, e.g., [21]–[24], or *ii*) machine learning (ML), where the classification is transparently made, and only the training and/or intelligence mechanism needs to be designed, e.g., [25]–[32].

In the case of ML-based classifiers, statistics/features such as root mean square delay spread (RMS-DS), maximum amplitude, rise time, received signal strength (RSS), and other similar metrics (mainly extracted from the channel impulse response (CIR)) are usually exploited. Authors in [25]–[30] relied on supervised learning algorithms. Specifically, statistical features of RSS measurements from WiFi signals are exploited in [25]. The spatial measurement diversity from multiple transmission reception points (TRPs) operating with TDOA is leveraged in [26]. However, LOS from several TRPs is required for the proposed method can effectively work. In [27], the training data and testing data sets are generated by a GNSS software receiver using intermediate frequency signal collected from an indoor pseudolite system. Meanwhile, ultra-wideband (UWB) systems are the focus in [28], [29]. CIR realizations are used for training a deep neural network in [28], while a hybrid deep learning and transfer learning method is proposed in [29]. A downsampled power delay profile, as a simpler alternative to the CIR, is proposed in [30] to feed a low-complexity deep neuronal network. On the other hand, unsupervised ML is proposed in [31], [32]. Specifically, an expectation maximization mechanism for Gaussian mixture models is developed in [31]. Therein, essential features of a UWB received signal, i.e., number of channel paths, mean excess delay, and RMS-DS, are used as input to the ML classifier. Meanwhile, a channel feature selection process is introduced in [32] to select only useful channel features to be used for the classification.

The main disadvantages of ML mechanisms, compared to threshold-based classifiers, are related to their data/time-hungry characteristics, complexity, and/or difficulty to probabilistically interpret the outputs. In case of threshold-based classifiers, authors in [21] modeled LOS and

NLOS hypothesis as being corrupted by additive noise with different probability distributions. They solved the binary hypothesis test under several assumptions. More recently, authors in [22], [23] exploited distance estimate residuals from multiple TRPs, however, as in [26], LOS from several TRPs is still a requirement. The average NLOS channel power per subcarrier is leveraged in [24] to perform LOS/NLOS link classification. Therein, NLOS links are discarded and a positioning decision is made taking into account only the measurements from those TRPs that establish LOS links with the user equipment (UE). However, authors in [24] may have implicitly assumed operation at regular microwave frequency bands since NLOS links are considered as multi-tap with no dominant tap. Then, given the use of a potentially massive number of antennas when operating at mm-wave or higher frequencies, NLOS links may exhibit a single or dominant tap, thus, their proposed framework cannot be, at least straightforwardly, applied in such case.

C. Contributions and Organization of the Paper

Similar to many of the aforementioned works, herein we propose a threshold-based LOS/NLOS classifier. However, we consider a single pair of TRPs connected through a single path, therefore, the mechanisms proposed in [22]–[24], [26] cannot be applied here. Moreover, our proposed classifier exploits an interesting physical phenomenon, which is that LOS and NLOS transmissions affect differently the polarization of receive signals. To the best of our knowledge, our proposal is the first one exploiting carrier phase measurements and polarization-diversity. Our specific contributions with respect to the state-of-the-art research are four-fold:

- We propose a threshold-based LOS/NLOS classifier exploiting transmit/receive polarization diversity. Specifically, an access point (AP) transmits a tone/carrier whose phase is measured at the UE over different polarization configurations. The relevant decision metric is conformed by weighted differential phase measurements. A LOS/NLOS decision is adopted after comparing such relevant metric to a decision threshold.
- We present different weighting configurations for the differential phase measurements. Specifically, the equal (EQU) weighting approach is noise-agnostic as it assigns equal weights to the differential phase measurements, while the more advanced minimum noise variance (MNV) and noise variance -proportional (NVP) weighting approaches exploit noise statistics and perform better. Their specific pros and cons are discussed and numerically validated. The NVP weighting approach is shown to outperform all the others, specially as one increases the number of signals/tones for the purpose of LOS/NLOS detection.

- We develop a framework for assessing the performance of the proposed LOS/NLOS classifier under different polarization-diversity and scenario configurations. Such framework includes a detailed characterization of the influence of LOS/NLOS propagation, AP and UE orientation, transmit/receive polarization, reflectors' electric properties, and signal strength on the carrier phase measurements. Our proposal can be applied to limited polarization-diversity systems (i.e., dual polarization at either transmitter or receiver);
- The simulation results reveal that: *i*) significant performance gains can be attained from properly weighting, e.g., via NVP, the differential carrier phase measurements and exploiting multi-signal/tone transmissions; *ii*) the performance of the proposed classifier depends critically on the NLOS environment (e.g., being seriously affected in case of scenarios with metallic reflectors); *iii*) the optimum decision threshold in terms of average error rate (AER) remains approximately the same independently of the material of potential NLOS reflectors, while it decreases following a power-law as the average path/link power gain increases; and *iv*) an inappropriate weighting of differential carrier phase measurements in a full polarization-diversity system, and also operating with limited diversity, degrades the classifier performance significantly.

The remainder of this paper is organized as follows. Section II introduces the system model and the problem of interest. In Section III, we characterize the propagation conditions under LOS and NLOS, and model the carrier phase measurements. Section IV presents and optimizes the proposed polarization diversity-enabled LOS/NLOS classifier exploiting carrier phase measurements. Finally, Section V presents numerical results, and Section VI concludes the article.

Notation: Boldface lowercase/uppercase letters denote column vectors/matrices, with the only exception of \mathbf{F}_u , which denotes a two-element field pattern vector by convention. Superscript $(\cdot)^T$ denotes the transpose operation, while $\|\cdot\|$ is the Euclidean norm of a vector, and $\|\cdot\|_F$ is the Frobenius norm of a matrix. \mathbb{C} , \mathbb{R} are respectively the set of complex and real numbers. Additionally, $\Pr(A)$ is the occurrence probability of event A , $\Pr(A|B)$ is the conditional occurrence probability of event A given the occurrence of event B , $\min\{\cdot\}$ is the minimum function, $\text{mod}(\cdot, \cdot)$ is the modulo operation, while $\Re\{\cdot\}$ and $\Im\{\cdot\}$ are respectively the real and imaginary part operators. Finally, $\arctan2(\cdot, \cdot)$ is the four-quadrant inverse tangent, which is given by

$$\arctan2(y, x) = 2 \arctan \frac{y}{\sqrt{x^2 + y^2} + x}. \quad (1)$$

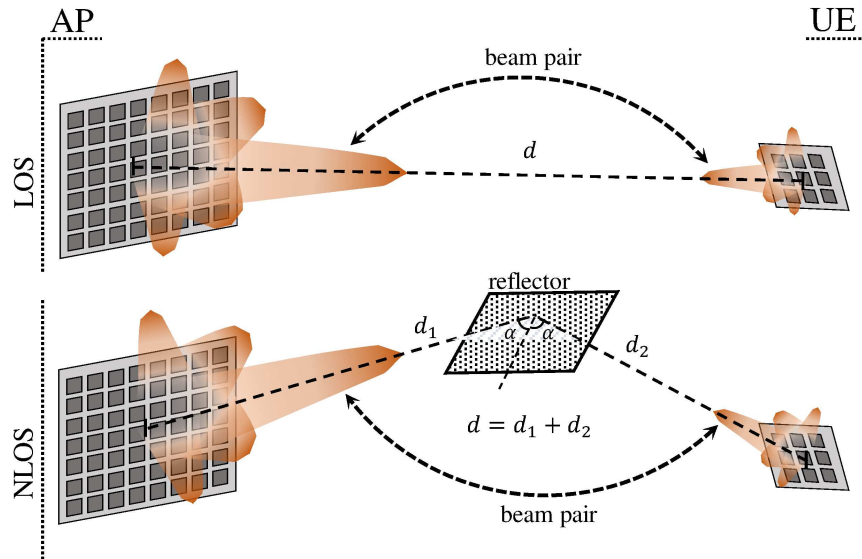


Fig. 1. System model: a) paired beams of AP and UE under LOS (top), and b) NLOS (bottom) conditions.

II. SYSTEM MODEL

Consider the system model illustrated in Fig. 1, where an AP, and a UE at an unknown position, have paired their main transmit/receive (mm-wave multi-antenna) beams. Beam management techniques, including beam establishment, beam refinement and beam tracking procedures, are usually exploited for this [33], [34]. Assume a single path, which can be either LOS (Fig. 1a) or NLOS (Fig. 1b) motivated by the use of massive transmit antenna arrays and mm-wave spectrum.¹ Moreover, the scattering phenomenon is ignored, although its effect could be included in the noise modeling introduced later in Section III-C. In fact, some numerical results on this are discussed in Section V-C. Finally, the length of the path, either direct (LOS) or reflected (NLOS), is denoted by d .

A. Channel Model and Polarization Configuration

We assume that both AP and UE are equipped with collocated vertically/horizontally-polarized antenna elements. Let \mathbf{F}_t and \mathbf{F}_r be the field pattern of the transmit and receive antennas, which respectively depend on the tuples (ϕ^t, θ^t) and (ϕ^r, θ^r) . Here, $\phi^t, \phi^r \in [-\pi, \pi]$ are the departure

¹In case the AP and UE are communicating through several beam pairs (single paths), one can still straightforwardly leverage our proposed method to classify them as LOS/NLOS.

and arrival azimuth angles, while $\theta^t, \theta^r \in [-\pi/2, \pi/2]$ are the departure and arrival elevation angles. The field patterns are two-element vectors containing the vertically and horizontally polarized component of the antenna array response as

$$\mathbf{F}_u = \begin{bmatrix} F_u^V(\phi^u, \theta^u) \\ F_u^H(\phi^u, \theta^u) \end{bmatrix}, \quad u \in \{t, r\}, \quad (2)$$

and they capture the (fixed) transmit/receive beamforming effects. Assuming a single (geometric) path, the electric field experienced by the receiver (at the output of the receive beamformer) can be written as

$$E_r = \sqrt{PZ_0} \mathbf{F}_r^T \mathbf{M} \mathbf{F}_t \exp\left(-j \frac{2\pi}{\lambda} d\right) = \zeta \mathbf{F}_r^T \mathbf{M} \mathbf{F}_t, \quad (3)$$

where P is the power gain of the path, $Z_0 = 120\pi$ is the characteristic impedance of vacuum, $\zeta \triangleq \sqrt{PZ_0} \exp(-j2\pi d/\lambda)$, and \mathbf{M} is the 2×2 polarization coupling matrix (Jones matrix), which describes how the path affects the polarization configuration.

Without loss of generality, we set the AP's antenna orientation axes as reference. The AP's antenna array lies in the yz -plane. Then, the 3D orientation of the UE's antenna array is defined by the Euler angles $\beta_x, \beta_y, \beta_z \in [-\pi/2, \pi/2]$ radians, which correspond to the angular rotation about axes x, y, z needed to match the orientation of the AP's antenna array. Moreover, the AP transmits a constant tone² at frequency f , with either a vertical or horizontal polarization at a time.

B. Goal & Hypothesis

In this work, we are concerned with the LOS/NLOS identification problem for a given single path (beam pair). Specifically, the goal is to determine whether:

H_0 : the beams are paired through a direct (LOS) path as in Fig. 1a; or

H_1 : the beams are paired through a reflected (NLOS) path as in Fig. 1b.

Note that a reflection modifies both the phase and amplitude of the incident polarized signal components, which can be exploited for LOS/NLOS identification. In the following, we illustrate this and specifically discuss how phase measurements can be leveraged.

²In practice, the continuous wave may originate directly from the local oscillator signal, or can be obtained by a FSK-modulation with a constant input (all 1s or 0s) [35] as in the Constant Tone Extension (CTE) signal from Bluetooth Core Specification 5.2 [36].

$$\begin{aligned}
\mathbf{Q}(\beta_x, \beta_y, \beta_z) &= \underbrace{\begin{bmatrix} \cos(-\beta_z) & -\sin(-\beta_z) & 0 \\ \sin(-\beta_z) & \cos(-\beta_z) & 0 \\ 0 & 0 & 1 \end{bmatrix}}_{\text{rotation matrix about } z} \underbrace{\begin{bmatrix} \cos(-\beta_y) & 0 & \sin(-\beta_y) \\ 0 & 1 & 0 \\ -\sin(-\beta_y) & 0 & \cos(-\beta_y) \end{bmatrix}}_{\text{rotation matrix about } y} \underbrace{\begin{bmatrix} 1 & 0 & 0 \\ 0 & \cos(-\beta_x) & -\sin(-\beta_x) \\ 0 & \sin(-\beta_x) & \cos(-\beta_x) \end{bmatrix}}_{\text{rotation matrix about } x} \\
&= \begin{bmatrix} \cos \beta_z & \sin \beta_z & 0 \\ -\sin \beta_z & \cos \beta_z & 0 \\ 0 & 0 & 1 \end{bmatrix} \begin{bmatrix} \cos \beta_y & 0 & -\sin \beta_y \\ 0 & 1 & 0 \\ \sin \beta_y & 0 & \cos \beta_y \end{bmatrix} \begin{bmatrix} 1 & 0 & 0 \\ 0 & \cos \beta_x & \sin \beta_x \\ 0 & -\sin \beta_x & \cos \beta_x \end{bmatrix} \\
&= \begin{bmatrix} \cos \beta_z \cos \beta_y & \sin \beta_z \cos \beta_x + \cos \beta_z \sin \beta_y \sin \beta_x & \sin \beta_z \sin \beta_x - \cos \beta_z \sin \beta_y \cos \beta_x \\ -\sin \beta_z \cos \beta_y & \cos \beta_z \cos \beta_x - \sin \beta_z \sin \beta_y \sin \beta_x & \cos \beta_z \sin \beta_x + \sin \beta_z \sin \beta_y \cos \beta_x \\ \sin \beta_y & -\cos \beta_y \sin \beta_x & \cos \beta_y \cos \beta_x \end{bmatrix} \quad (5)
\end{aligned}$$

III. PROPAGATION AND PHASE MEASUREMENTS

A. LOS Propagation

It is shown in [37] that under LOS conditions the polarization coupling matrix has the form of a rotation matrix with rotation angle ϑ , thus,

$$\mathbf{M} = \begin{bmatrix} \cos \vartheta & \sin \vartheta \\ -\sin \vartheta & \cos \vartheta \end{bmatrix}. \quad (4)$$

Next, we illustrate how ϑ can be obtained. First, let us define $\mathbf{Q} \in \mathbb{R}^{3 \times 3}$ as shown in (5) at the top of the page to describe the axis orientation change of the receive antenna (which lies on its local xz plane) with respect to the transmit antenna in 3D space. Let \mathbf{o}_r be the receive orientation vector (e.g., $[1, 0, 0]^T$ and $[0, 1, 0]^T$ for vertically and horizontally-polarized receptions, respectively). Then, the transformed orientation vector in global coordinates is given by

$$\bar{\mathbf{o}}_r = \mathbf{Q} \mathbf{o}_r. \quad (6)$$

Now, we rotate the orientation vector by $p = -\phi^r - \pi/2$ in the azimuth direction and $q = \theta^r$ in the elevation direction to match the orientation of the transmitter (thus, the wave travel direction lies now in the y -direction) as

$$\tilde{\mathbf{o}}_r = \begin{bmatrix} \cos p & -\sin p & 0 \\ \cos q \sin p & \cos q \cos p & -\sin q \\ \sin q \sin p & \sin q \cos p & \cos q \end{bmatrix} \bar{\mathbf{o}}_r = - \begin{bmatrix} \sin \phi^r & -\cos \phi^r & 0 \\ \cos \theta^r \cos \phi^r & \cos \theta^r \sin \phi^r & \sin \theta^r \\ \sin \theta^r \cos \phi^r & \sin \theta^r \sin \phi^r & -\cos \theta^r \end{bmatrix} \bar{\mathbf{o}}_r. \quad (7)$$

Since the projection plane lies in the xz plane due to the placement of the transmitter, we simply omit the y -component of $\tilde{\mathbf{o}}_r$, and calculate the projection of the orientation vector on the projection plane as

$$\mathbf{p}_r = \frac{\mathbf{A}_{xz}\tilde{\mathbf{o}}_r}{\|\mathbf{A}_{xz}\tilde{\mathbf{o}}_r\|}, \quad (8)$$

where $\mathbf{A}_{xz} = \begin{bmatrix} 1 & 0 & 0 \\ 0 & 0 & 1 \end{bmatrix}$. Meanwhile, the transmit polarization vector is given by

$$\mathbf{p}_t = \frac{\mathbf{F}_t}{\|\mathbf{F}_t\|}, \quad (9)$$

while the angle between transmit and receive polarization vectors obeys

$$\psi = \arccos(\mathbf{p}_t^T \mathbf{p}_r). \quad (10)$$

The difference between angles

$$\varpi_t = \arctan2(F_t^H(\phi^r, \theta^r), F_t^V(\phi^t, \theta^t)), \quad (11)$$

$$\varpi_r = \arctan2(F_r^H(\phi^r, \theta^r), F_r^V(\phi^t, \theta^t)) \quad (12)$$

represents the polarization mismatch between the receive and transmit antenna if both were aligned on the same optical axis. Note that ψ , however, takes the different orientation of the receive antenna into account. Finally, one obtains

$$\vartheta = \varpi_t - \varpi_r - \psi. \quad (13)$$

The entire above process is illustrated geometrically in Fig. 2.

B. NLOS Propagation

Assume for simplicity a single-reflection path in the NLOS scenario. The reflecting surface is rotated about axes x, y, z by $\delta_x, \delta_y, \delta_z \in [-\pi/2, \pi/2]$ radians (Euler angles) with respect to the AP antennas. Then, under the NLOS hypothesis, the polarization coupling matrix has the form

$$\mathbf{M} = \underbrace{\begin{bmatrix} \cos \vartheta_2 & \sin \vartheta_2 \\ -\sin \vartheta_2 & \cos \vartheta_2 \end{bmatrix}}_{\substack{\text{rotation matrix:} \\ \text{reflector-UE}}} \underbrace{\begin{bmatrix} R_{\perp} & 0 \\ 0 & R_{\parallel} \end{bmatrix}}_{\text{reflection matrix}} \underbrace{\begin{bmatrix} \cos \vartheta_1 & \sin \vartheta_1 \\ -\sin \vartheta_1 & \cos \vartheta_1 \end{bmatrix}}_{\substack{\text{rotation matrix:} \\ \text{AP-reflector}}}, \quad (14)$$

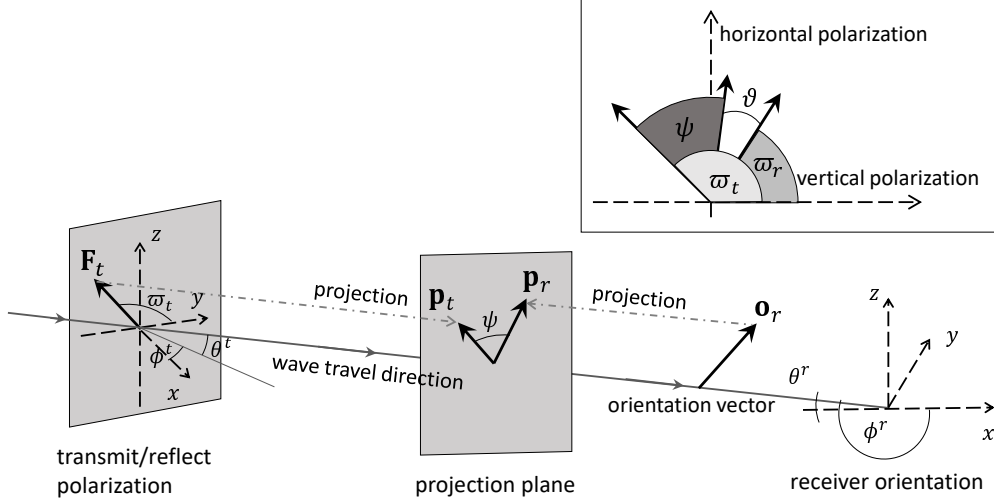


Fig. 2. Illustration of the geometric polarization [37].

where ϑ_1 and ϑ_2 are the rotation angles for the incident and reflected electromagnetic fields, respectively. Similarly, R_{\parallel} and R_{\perp} are the parallel and perpendicular reflection coefficients of the reflector, respectively. The reflection coefficients are defined as [38]

$$R_{\perp} = \frac{\cos \alpha - \sqrt{\varepsilon - \sin^2 \alpha}}{\cos \alpha + \sqrt{\varepsilon - \sin^2 \alpha}}, \quad (15)$$

$$R_{\parallel} = \frac{\varepsilon \cos \alpha - \sqrt{\varepsilon - \sin^2 \alpha}}{\varepsilon \cos \alpha + \sqrt{\varepsilon - \sin^2 \alpha}}, \quad (16)$$

where $\varepsilon = \varepsilon_r - j60\kappa\lambda$, α is the angle of incidence as illustrated in Fig. 1, and ε_r and κ are the normalized relative dielectric constant and the conductivity of the reflecting surface at the operation frequency, respectively.³ Observe that NLOS converges LOS for $\alpha = \pi/2$, for which we can write (14) as (4) with $\vartheta = \vartheta_1 + \vartheta_2$.

Table I compiles the electric properties of some materials that appear commonly as reflectors in wireless communication networks. Their corresponding parallel and perpendicular reflection coefficients are respectively plotted in Fig. 3 and Fig. 4 as a function of the angle of incidence α . Note that α depends not only on the transmit antenna, receive antenna, and reflector orientations, but also on their corresponding positions. Later, in Section V, we generate random values for α to account for different node deployment scenarios.

³At sufficiently high frequencies, even a metal behaves as a dielectric [39].

TABLE I
ELECTRIC PROPERTIES OF THE CONSIDERED REFLECTORS [39]–[42].

Materials	ϵ_r	κ (S/m)
glass	6	10^{-14}
wood	1.2	10^{-4}
moist concrete	2.3	10^{-2}
distilled water	4	5
conductor (metal-like/alloys)	30	10

The rotation angles ϑ_1 and ϑ_2 in (14) can be obtained by treating the reflecting surface as a virtual antenna and exploiting the framework in Section III-A. By doing this, Fig. 2 can be re-utilized to visualize/understand the polarization changes undergone over each, the incident and reflected, path component.

1) *On the computation of ϑ_1* : The reflecting surface is modeled as a virtual receive antenna with arrival azimuth and elevation angles α and $\theta_t - \delta_x$, respectively. Then, ϑ_1 can be obtained by following the procedure for computing (13) but using $\mathbf{Q}(\delta_x, \delta_y, \delta_z)$ when evaluating (5), and setting $\phi_r \leftarrow \alpha$ and $\theta_r \leftarrow \theta_t - \delta_x$.

2) *On the computation of ϑ_2* : The reflecting surface is modeled as a virtual transmit antenna. Then, ϑ_2 can be obtained by following the procedure for computing (13) but using $\mathbf{Q}(\beta_x - \delta_x, \beta_y - \delta_y, \beta_z - \delta_z)$ when evaluating (5).

C. Carrier Phase Measurements

Assume that the UE employs a phase-locked loop (PLL) circuit to track the phase of the tone sent by the AP at frequency f . Moreover, the AP and the UE are clock-synchronized. Then, the phase measurements at the UE can be written as

$$\varphi = \text{mod}\left(\frac{2\pi}{\lambda}d + \tilde{\varphi} + \bar{\varphi}, 2\pi\right), \quad (17)$$

where $\tilde{\varphi}$ is the phase measurement noise and $\bar{\varphi}$ is the phase shift introduced by the polarization configuration and/or NLOS reflections. The measurement noise is modeled as a zero mean normal distribution, i.e., $\tilde{\varphi} \sim \mathcal{N}(0, \sigma)$, with the standard deviation given by [43, eq. (1.15)]

$$\sigma = \sqrt{\frac{1}{\gamma} \left(1 + \frac{1}{TB\gamma}\right)}. \quad (18)$$

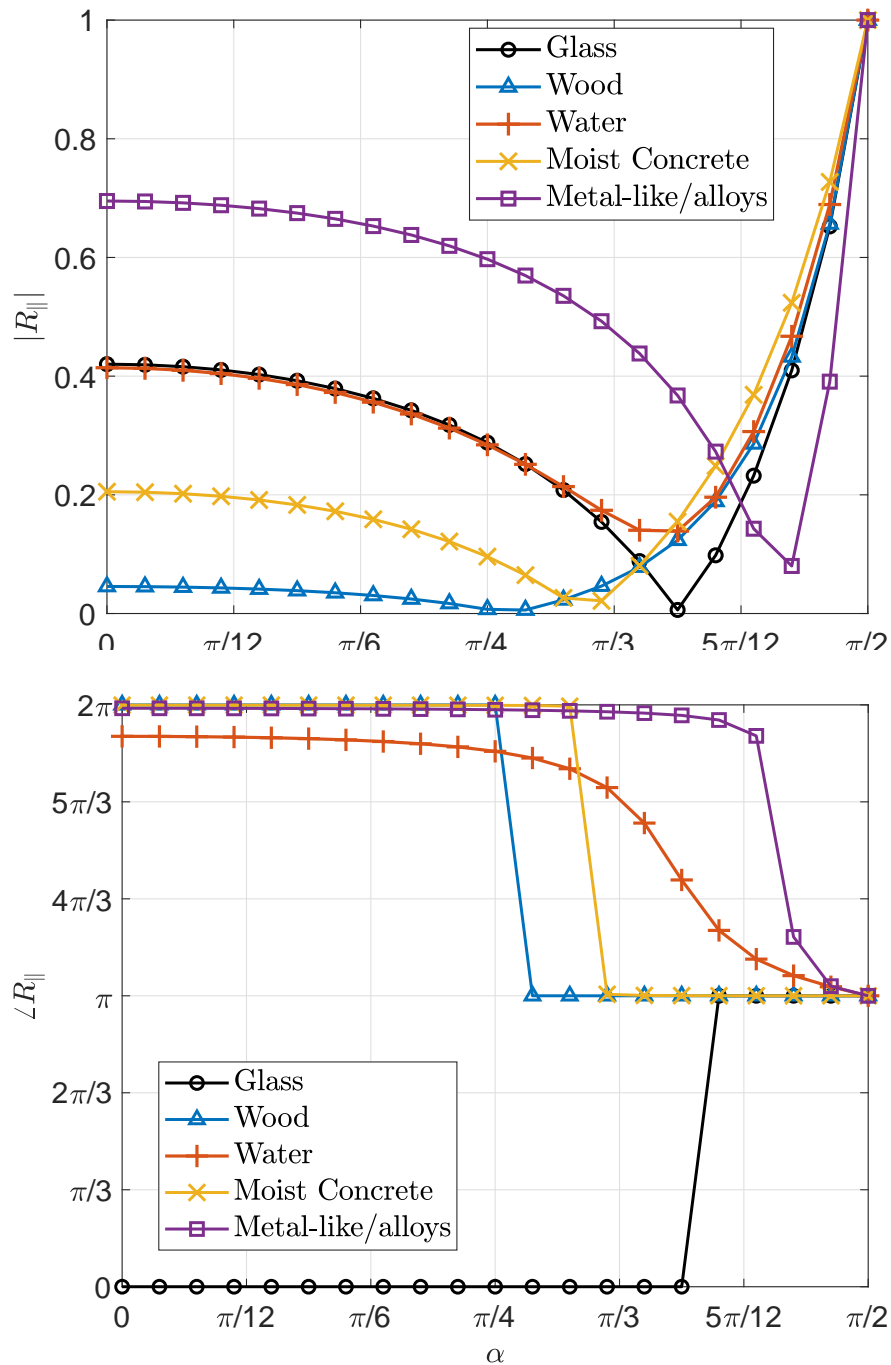


Fig. 3. Parallel reflection coefficient of materials in Table I as a function of incidence angle α and specified by b) amplitude (top) and phase (bottom).

Here, B is the bandwidth of the loop filter, and T is the integration time. Meanwhile, γ is the signal-to-noise ratio (SNR) at the received antenna, and it is given by [44, Ch.2]

$$\gamma = \frac{G\lambda^2 |E_r|^2}{480\pi^2 B N_0}, \quad (19)$$

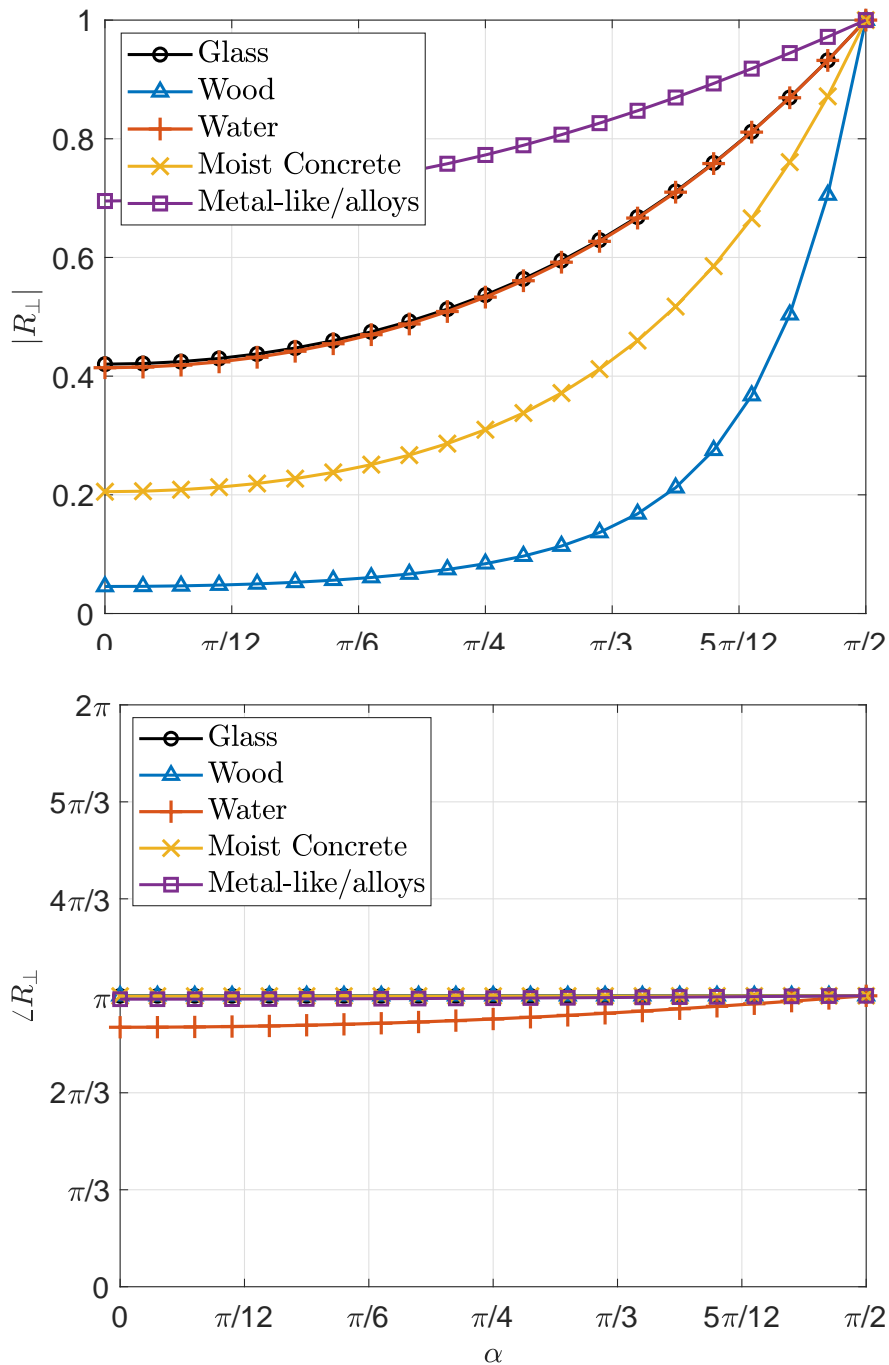


Fig. 4. Perpendicular reflection coefficient of materials in Table I as a function of incidence angle α and specified by b) amplitude (top) and phase (bottom).

where N_0 is the noise spectral density, and G is the UE's antenna gain. Finally, $\bar{\varphi}$ is given by

$$\bar{\varphi} = \arctan2(\Im\{\mathbf{F}_r^T \mathbf{M} \mathbf{F}_t\}, \Re\{\mathbf{F}_r^T \mathbf{M} \mathbf{F}_t\}). \quad (20)$$

IV. HYPOTHESIS TESTING DESIGN

The experiment is designed as follows. AP's/UE's antennas can be configured to transmit/receive with either horizontal (H) or vertical (V) polarization. Thus, there are 4 or 2 possible combinations in a full-diversity (where both transmit and receive antennas are dual-polarized) or transmit/receive (only)-diversity system, respectively. Let us use the super-index pair (p, q) with $p, q \in \{H, V\}$ to denote each of above polarization configurations. In this case, p and q and correspond to the receive and transmit polarization configuration, respectively. Now, we define matrix \mathbf{E}_r to collect all the possible polarization configurations as

$$\mathbf{E}_r = \begin{bmatrix} E_r^{V,V} & E_r^{V,H} \\ E_r^{H,V} & E_r^{H,H} \end{bmatrix}. \quad (21)$$

Note that a pure vertical, horizontal configuration implies that $\mathbf{F}_u = [F_u^V(\phi^u, \theta^u), 0]^T$, $\mathbf{F}_u = [0, F_u^H(\phi^u, \theta^u)]^T$, respectively. Therefore, for each possible polarization configuration the rotation angle may be different (ϑ for LOS, and ϑ_1, ϑ_2 for NLOS, are different). Finally, carrier phase measurements are collected using a time-division protocol, i.e., measuring over one polarization configuration at a time.

A. LOS/NLOS Hypothesis

By substituting (4) into (3) for each possible polarization configuration, one obtains

$$\mathbf{E}_r^{\text{los}} = \zeta \begin{bmatrix} \eta_1 \cos \vartheta^{V,V} & \eta_2 \sin \vartheta^{V,H} \\ -\eta_3 \sin \vartheta^{H,V} & \eta_4 \cos \vartheta^{H,H} \end{bmatrix} \quad (22)$$

under LOS propagation conditions, where

$$\eta_1 \triangleq F_r^V(\phi^r, \theta^r) F_t^V(\phi^t, \theta^t), \quad (23a)$$

$$\eta_2 \triangleq F_r^V(\phi^r, \theta^r) F_t^H(\phi^t, \theta^t), \quad (23b)$$

$$\eta_3 \triangleq F_r^H(\phi^r, \theta^r) F_t^V(\phi^t, \theta^t), \quad (23c)$$

$$\eta_4 \triangleq F_r^H(\phi^r, \theta^r) F_t^H(\phi^t, \theta^t). \quad (23d)$$

Similarly to (22), one can obtain $\mathbf{E}_r^{\text{nlos}}$ in (24) (at the top of the next page) under NLOS propagation conditions by substituting (14) into (3). Finally, we force $\eta_1, \eta_2, \eta_3, \eta_4 \in \mathbb{R}^+$ by conveniently compensating the phase shifts introduced by transmit/receive beamformers.

$$\mathbf{E}_r^{\text{nlos}} = \zeta \begin{bmatrix} \eta_1(-R_{\parallel} \sin \vartheta_1^{V,V} \sin \vartheta_2 + R_{\perp} \cos \vartheta_1^{V,V} \cos \vartheta_2^{V,V}) & \eta_2(R_{\parallel} \cos \vartheta_1^{V,H} \sin \vartheta_2^{V,H} + R_{\perp} \sin \vartheta_1^{V,H} \cos \vartheta_2^{V,H}) \\ -\eta_3(R_{\parallel} \sin \vartheta_1^{H,V} \cos \vartheta_2^{H,V} + R_{\perp} \cos \vartheta_1^{H,V} \sin \vartheta_2^{H,V}) & \eta_4(R_{\parallel} \cos \vartheta_1^{H,H} \cos \vartheta_2^{H,H} - R_{\perp} \sin \vartheta_1^{H,H} \sin \vartheta_2) \end{bmatrix}. \quad (24)$$

B. Relevant Decision Metric

We assume the UE's antenna array rotation configuration is unknown⁴, and propose the following relevant decision metric based on differential measurements

$$\Delta_i = \text{mod} \left([\varphi^{V,V-}, \varphi^{V,H}, \varphi^{V,V-}, \varphi^{H,V}, \varphi^{V,V-}, \varphi^{H,H}, \varphi^{V,H-}, \varphi^{H,V}, \varphi^{V,H-}, \varphi^{H,H}, \varphi^{H,V-}, \varphi^{H,H}]^T + \pi \boldsymbol{\nu}_i, 2\pi \right). \quad (25)$$

Here, $\boldsymbol{\nu}_i \in [0, 1]^{6 \times 1}$ is a binary 6-element vector representation of the decimal number i , thus, $i \in \{0, 1, 2, \dots, 2^6 - 1\}$. For instance, $\boldsymbol{\nu}_4 = [0, 0, 0, 1, 0, 0]^T$, while $\boldsymbol{\nu}_{19} = [0, 1, 0, 0, 1, 1]^T$. Observe that Δ_i in (25) exploits the measurements over all the four polarization configurations and removes the impact of the phase shift introduced by the path distance d , which is unknown. The role of $\pi \boldsymbol{\nu}_i$ in (25) is explained next.

Observe that $\mathbf{E}_r^{\text{los}}/\zeta \in \mathbb{R}^{2 \times 2}$, while $\mathbf{E}_r^{\text{nlos}}/\zeta \in \mathbb{C}^{2 \times 2}$ due to complex valued reflection coefficients (15), (16). This means that the set of phase shifts that can be potentially introduced under NLOS propagation conditions is infinite, i.e., $\bar{\varphi} \in [0, 2\pi]$, while they are limited to $\bar{\varphi} \in \{0, \pi\}$ under LOS. Then, under LOS conditions, there is a vector $\pi \boldsymbol{\nu}_i = [0, \pi]^{6 \times 1}$ that ideally drives (25) to zero. In other words, under LOS conditions and perfect measurements, one obtains $\Delta_i = 0$ for a certain $i \in \{0, 1, 2, \dots, 63\}$ according to the specific UE's antenna rotation configuration. Meanwhile, under NLOS conditions, Δ_i depends on the specific reflector orientation and reflection coefficients, thus, will be surely different than 0 independently of the UE's antenna array rotation configuration. In all cases, the common (path) phase shift $2\pi d/\pi$ is removed by the differential operation.

Based on the above formulation, the hypothesis testing can be designed such that

$$\min_i \|\Delta_i\| = 0 \text{ implies LOS } (H_0), \text{ while}$$

⁴Note that in scenarios where the UE is aware of the AP's antenna orientation and it is equipped with proper sensing mechanisms, e.g., gyroscope and geomagnetic sensors, the value of $\beta_x, \beta_y, \beta_z$ may be (approximately) known beforehand. Nevertheless, in such scenarios, one needs to consider the noise effects related to the estimation of these parameters, which may be significant if the UE is a low-capability device.

$\min_i \|\Delta_i\|^2 > 0$ indicates NLOS (H_1).

However, in practice, measurements are imperfect due to noise effect and non-modeled phenomena such as scattering. Therefore, the hypothesis needs to be relaxed as

$$\begin{cases} \min_i \|\mathbf{W} \hat{\Delta}_i\|^2 \leq \xi, & \rightarrow \text{declare LOS } (H_0) \\ \min_i \|\mathbf{W} \hat{\Delta}_i\|^2 > \xi, & \rightarrow \text{declare NLOS } (H_1) \end{cases}, \quad (26)$$

where $\hat{\Delta}_i$ denotes the estimation of Δ_i based on measurements, and ξ is a decision threshold. The greater the threshold value is, the greater the LOS detection probability is, but also false-alarm probabilities become more prominent. Moreover, \mathbf{W} is a diagonal real weighting matrix with entries $w_j, j = 1, \dots, 6$ and $\|\mathbf{W}\|_F^2 = \sum_{j=1}^6 w_j^2 = 1$ enabling a differential treatment of the elements of Δ . Observe that by zeroing a certain w_j , one can null the effect of any of the elements of Δ_i . This can be exploited for assessing the performance of systems with either Tx or Rx polarization diversity. We provide some numerical discussions on this in Section V.

A downside of the above approach is that $\Im\{\mathbf{E}_r^{\text{los}}/\zeta\}, \Re\{\mathbf{E}_r^{\text{los}}/\zeta\} \approx 0$ for a wide range of reflection-related parameters. This is because $60\kappa\lambda$ in ε (check (15) and (16)) is very small at the mm-wave spectrum operation (i.e., small λ) and/or when reflectors are dielectric (i.e., small κ). In such scenarios, the angle of $\mathbf{E}_r^{\text{los}}$ is very close to 0 or π , which affects considerably the performance of a detector based on (25)–(26). We address this issue as discussed in the following.

Note that not all $\nu_i, i = 0, \dots, 63$, need to be evaluated in LOS scenarios due to some geometric relations that can be exploited. Specifically, $\vartheta^{V,V} = \vartheta^{V,H}$ and $\vartheta^{H,V} = \vartheta^{H,H}$ holds under LOS, while there are even some spatial geometric relationships between $\vartheta^{V,V}$ and $\vartheta^{H,H}$ which are difficult to derive in closed-form, but can be obtained numerically using the framework in Section III-A. In a nutshell, there are some vectors ν_i that would never make $\Delta_i = \mathbf{0}$ when operating in LOS conditions. In fact, it can be shown that out of the 64 possible vectors ν_i , one (and only one) of the 8 following vectors: $\nu_0, \nu_{11}, \nu_{21}, \nu_{30}, \nu_{38}, \nu_{45}, \nu_{51}, \nu_{56}$, makes $\Delta_i = \mathbf{0}$ in LOS conditions with perfect phase measurements. Therefore, we use only these vectors when evaluating (25).

C. On the Weights Configuration

By substituting (17) into (25), one obtains

$$\begin{aligned} \hat{\Delta}_i = \text{mod} \left(& [\tilde{\varphi}^{V,V} + \bar{\varphi}^{V,V} - \tilde{\varphi}^{V,H} - \bar{\varphi}^{V,H}, \tilde{\varphi}^{V,V} + \bar{\varphi}^{V,V} - \tilde{\varphi}^{H,V} - \bar{\varphi}^{H,V}, \\ & \tilde{\varphi}^{V,V} + \bar{\varphi}^{V,V} - \tilde{\varphi}^{H,H} - \bar{\varphi}^{H,H}, \tilde{\varphi}^{V,H} + \bar{\varphi}^{V,H} - \tilde{\varphi}^{H,V} - \bar{\varphi}^{H,V}, \\ & \tilde{\varphi}^{V,H} + \bar{\varphi}^{V,H} - \tilde{\varphi}^{H,H} - \bar{\varphi}^{H,H}, \tilde{\varphi}^{H,V} + \bar{\varphi}^{H,V} - \tilde{\varphi}^{H,H} - \bar{\varphi}^{H,H}]^T + \pi \boldsymbol{\nu}_i, 2\pi \right). \end{aligned} \quad (27)$$

Note that due to the intricacy of (24), and the several unknowns, i.e., R_{\parallel} , R_{\perp} and reflector orientation, it becomes cumbersome getting specific insights for the attainable values of $\min_i \|\mathbf{W} \hat{\Delta}_i\|^2$ for the NLOS scenario. Therefore, we focus merely on the LOS scenario in the following.

Under LOS conditions, we have that

$$\begin{aligned} & [\bar{\varphi}^{V,V} - \bar{\varphi}^{V,H}, \bar{\varphi}^{V,V} - \bar{\varphi}^{H,V}, \bar{\varphi}^{V,V} - \bar{\varphi}^{H,H}, \bar{\varphi}^{V,H} - \bar{\varphi}^{H,V}, \\ & \bar{\varphi}^{V,H} - \bar{\varphi}^{H,H}, \bar{\varphi}^{H,V} - \bar{\varphi}^{H,H}]^T + \pi \boldsymbol{\nu}_i = \mathbf{0} \end{aligned} \quad (28)$$

for a certain $i \in \{0, 11, 21, 30, 38, 45, 51, 56\}$. Then, by leveraging (28) when evaluating (27), and expanding the squared norm, one obtains

$$\begin{aligned} \min_i \|\mathbf{W} \hat{\Delta}_i\|^2 = & w_1^2 (\tilde{\varphi}^{V,V} - \tilde{\varphi}^{V,H})^2 + w_2^2 (\tilde{\varphi}^{V,V} - \tilde{\varphi}^{H,V})^2 + w_3^2 (\tilde{\varphi}^{V,V} - \tilde{\varphi}^{H,H})^2 \\ & + w_4^2 (\tilde{\varphi}^{V,H} - \tilde{\varphi}^{H,V})^2 + w_5^2 (\tilde{\varphi}^{V,H} - \tilde{\varphi}^{H,H})^2 + w_6^2 (\tilde{\varphi}^{H,V} - \tilde{\varphi}^{H,H})^2 \end{aligned} \quad (29)$$

assuming LOS and relatively accurate phase measurements. In the following, we discuss three different weighting approaches.

1) *Equal (EQU) weighting*: This is the simplest approach. Each addend element of $\hat{\Delta}_i$ is equally weighted, thus,

$$w_j = 1/\sqrt{6}, \quad \forall j. \quad (30)$$

2) *Minimum noise variance (MNV) weighting*: Intuitively, a proper weights configuration should take into account the measurements accuracy. Assume that the noise statistics of the measurements, specifically the variances, are known. Indeed, they can be readily estimated based on SNR measurements followed by the evaluation of (18). Now, observe that by departing from (29), one can write

$$\mathbb{E} \left[\min_i \|\mathbf{W} \hat{\Delta}_i\|^2 \right] = \sum_{j=1}^6 \sigma_j^2 w_j^2, \quad (31)$$

where

$$\sigma_1^2 \triangleq (\sigma^{V,V})^2 + (\sigma^{V,H})^2, \quad (32a)$$

$$\sigma_2^2 \triangleq (\sigma^{V,V})^2 + (\sigma^{H,V})^2, \quad (32b)$$

$$\sigma_3^2 \triangleq (\sigma^{V,V})^2 + (\sigma^{H,H})^2, \quad (32c)$$

$$\sigma_4^2 \triangleq (\sigma^{V,H})^2 + (\sigma^{H,V})^2, \quad (32d)$$

$$\sigma_5^2 \triangleq (\sigma^{V,H})^2 + (\sigma^{H,H})^2, \quad (32e)$$

$$\sigma_6^2 \triangleq (\sigma^{H,V})^2 + (\sigma^{H,H})^2. \quad (32f)$$

Based on standard convex optimization techniques exploiting, for instance, Karush–Kuhn–Tucker (KKT) conditions, it can be easily shown that the weights configuration that minimizes (31) subject to $\sum_{j=1}^6 w_j^2 = 1$ is given by

$$w_j^* = \begin{cases} 1, & \text{for } j = \arg \min_z \sigma_z^2 \\ 0, & \text{otherwise.} \end{cases} \quad (33)$$

This is, only the term of (29) with the best expected accuracy is considered for the LOS/NLOS detection.

3) *Noise variance -proportional (NVP) weighting*: The main problem with the MNV approach is that it seriously constrains the exploitation of ν_i for LOS/NLOS detection. Note that five out of the six elements of ν_i are neglected when using MNV weighting, thus, one cannot take full advantage of its particular construction structure for noise mitigation. Herein, we circumvent this issue by adopting squared weights proportional to the noise variances. Specifically,

$$w_j^* = \mu / \sigma_j, \quad (34)$$

where μ is a normalization factor that guarantees $\sum_{j=1}^6 w_j^2 = 1$, thus, it is given by

$$\mu = \frac{1}{\sqrt{\sum_{j=1}^6 \sigma_j^{-2}}}. \quad (35)$$

In this way, the noisier elements of $\hat{\Delta}_i$ weigh less, but they are never neglected unless operating in the high SNR asymptotic regime.

The LOS/NLOS detection performance under each of the above weights configurations is numerically assessed in the next section.

V. NUMERICAL RESULTS

Here, we numerically illustrate the performance of the proposed LOS/NLOS identification method. We produce 10^5 scenario instances comprising LOS and NLOS configurations with equal probability. We generate $\alpha \in [0, \pi/2]$, $\phi^t, \phi^r \in [-\pi, \pi]$, $\theta^t, \theta^r \in [-\pi/2, \pi/2]$, and $\beta_x, \beta_y, \beta_z, \delta_x, \delta_y, \delta_z \in [-\pi, \pi]$ uniformly random, and set $B = 20$ Hz, $T = 10$ ms, $N_0 = 10^{-20.38}$ W/Hz assuming ambient temperature of 300 K, $G = 0$ dB, $f = 30$ GHz. Finally, we assume $F_u^H(\phi^u, \theta^u) = 1$ and $F_u^V(\phi^u, \theta^u) = 1$ for horizontally and vertically polarized transmissions ($u = t$) or receptions ($u = r$) such that the spatial antenna gains/losses (antenna pattern) are ignored or counteracted by beamforming gains.

A. On the Probabilities of Miss Detection and False Alarm

Herein, we assess the performance of the proposed detection mechanism by evaluating the probability of miss-detection (PMD) and probability of false alarm (PFA). Specifically, the LOS – PMD and PFA are respectively given by

- the probability of declaring NLOS given LOS conditions: $\Pr(H_1|H_0)$;
- the probability of declaring LOS given NLOS conditions: $\Pr(H_0|H_1)$.

Observe that LOS – PMD and PFA match respectively NLOS – PFA and PMD, thus, we merely focus on the former in the following.

Fig. 5 evaluates the performance of a full-diversity system (both transmit and receive polarization diversity) as a function of the decision threshold ξ . Herein, we adopt the NVP weighting approach, while the EQU and MNV weighting configurations and their relative performance are analyzed later in Section V-B. In case of NLOS, a reflector is assumed composed of one of the materials given in Table I. In addition, we show the performance for a randomly chosen (among those listed in Table I) material. Specifically, Fig. 5a shows the LOS – PMD and PFA, while Fig. 5b averages both metrics to illustrate the average error rate (AER) performance metric as

$$\begin{aligned} \text{AER} &= \Pr(H_1|H_0) \Pr(H_0) + \Pr(H_0|H_1) \Pr(H_1) \\ &= 0.5 \times (\Pr(H_1|H_0) + \Pr(H_0|H_1)), \end{aligned} \quad (36)$$

where in the last step, we exploit $\Pr(H_0) = \Pr(H_1) = 0.5$.

Observe that in LOS scenarios there are no reflectors, thus, there is a unique curve for the LOS – PMD in Fig. 5a. Meanwhile, the LOS – PFA is different for each reflecting material

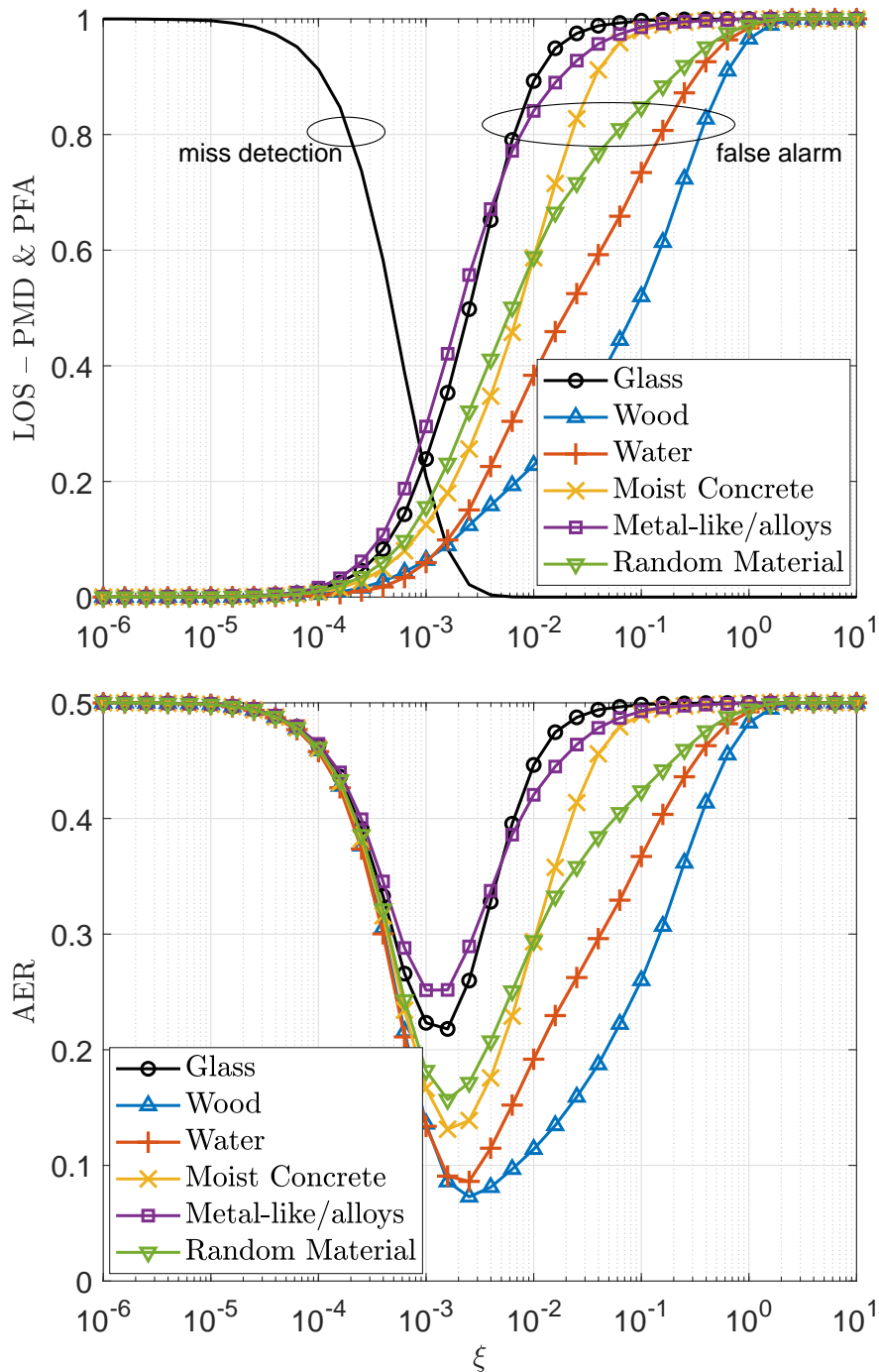


Fig. 5. a) LOS - PMD and PFA (top), and b) AER (bottom) as a function of ξ . We use the NVP weighting approach, and set $P = -100$ dB.

as it depends on its corresponding electric characteristics $\{\epsilon_r, \kappa\}$, which influence differently the reflection coefficients $\{R_{\perp}, R_{\parallel}\}$ as illustrated in Fig. 3. The detection capabilities in an environment with wooden reflectors and reflecting water are superior than in the other considered

environments, specially compared to that with metallic reflectors. The reasons for this can be obtained from Fig. 3. Note that wooden reflectors introduce considerable power losses to both polarization components of the incident signal, thus, promoting more noisy measurements in NLOS conditions. In case of reflecting water, the performance gains come from the continuous range of phase shifts (instead of approximately discrete as for other materials) that are introduced during the reflection of both vertically and horizontally polarized signal components. As corroborated in Fig. 5b, the relative performance in terms of AER is determined by the LOS – PFA. Interestingly, the optimum decision threshold remains around the same value for all the considered (heterogeneous) reflecting materials, i.e., $10^{-3} \leq \xi^{\text{opt}} \leq 3 \times 10^{-3}$, although being slightly larger for reflecting materials promoting better performance, e.g., wood and water.

B. On the Performance Impact of the Path Power Gain, Limited-Diversity and Weights Configuration

In the following, we focus only on the AER metric. Specifically, we illustrate the performance of the optimum AER, which is the minimum achievable AER for any ξ . We evaluate the performance of a limited-diversity system, where one of the link sides is assumed equipped with just a horizontally-polarized antenna. The corresponding performance can be easily evaluated using the full-diversity simulation framework but with:

- $\mathbf{W} = \text{diag}([0, 0, 0, 0, 0, 1])$ for transmit (TX)-diversity,
- $\mathbf{W} = \text{diag}([0, 0, 0, 0, 1, 0])$ for receive (RX)-diversity.

Moreover, we select a random material among those given in Table I for each NLOS scenario instance.

Fig. 6 illustrates the system performance as a function of the path power gain P . Obviously, the AER performance improves as P increases as corroborated in Fig. 6a. However, the improvement rate is relatively slow for $P \geq -120$ dB. Indeed, the AER decreases approximately only 0.1 units by increasing the path power gain from -120 dB to -70 dB. Note that a full-diversity system with EQU weighting does not provide significant performance improvements compared to a limited diversity system. Remarkably, significant performance gains are attainable by exploiting the statistics of the noise measurements, especially via NVP weighting. Indeed, a full-diversity system with NVP weighting can significantly outperform all the other configurations, including that one with MNV weighting. Meanwhile, the RX-diversity outperforms the TX-diversity

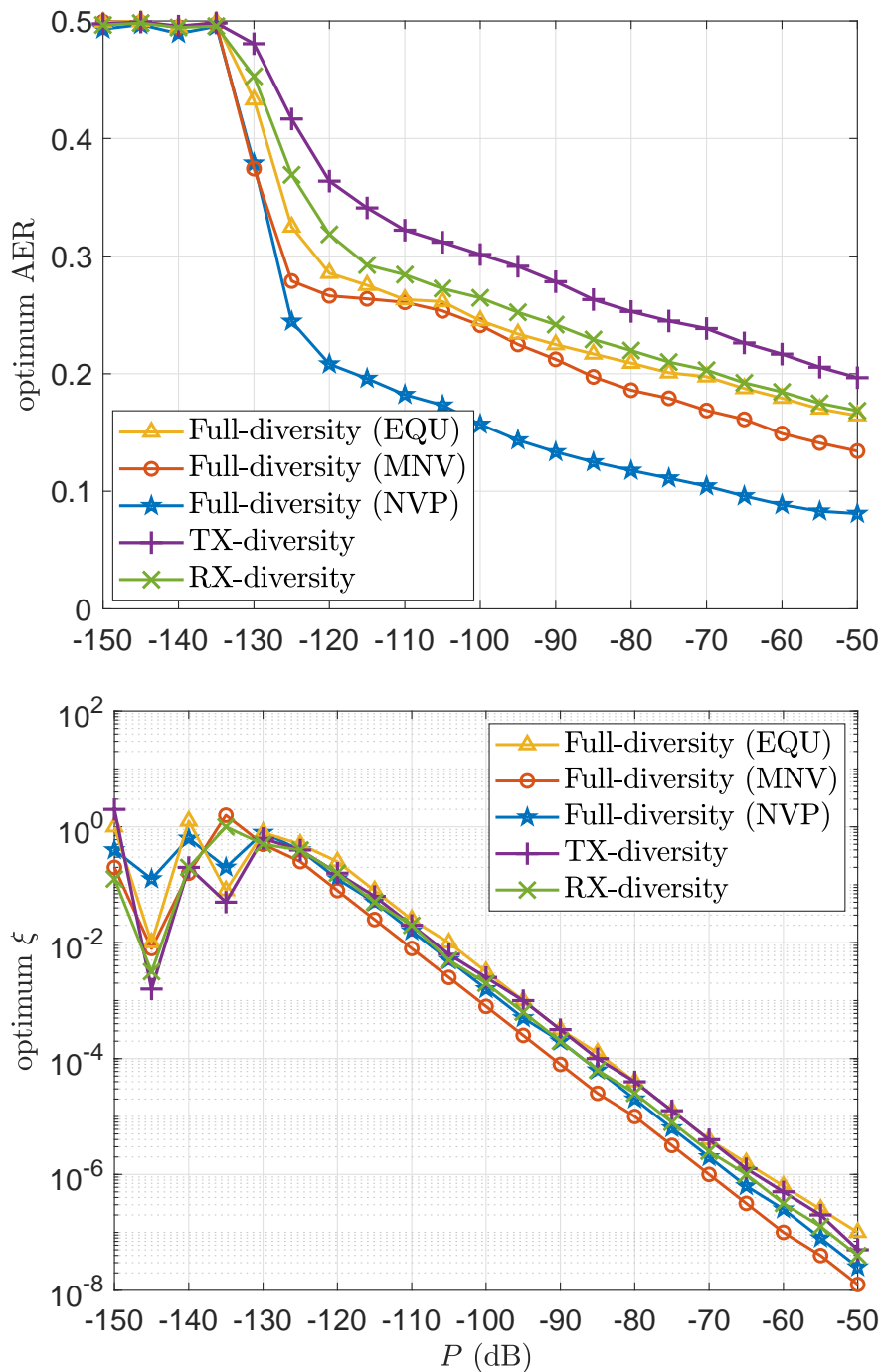


Fig. 6. a) Optimum AER (top), and b) corresponding ξ (bottom) as a function of the path power gain. In NLOS scenarios, the reflecting material is selected randomly among those given in Table I.

system, which may influence the link orientation design for LOS/NLOS identification in limited-diversity systems. Related to the decision threshold, Fig. 6b evinces that the optimum ξ , i.e., the one that minimizes the AER, remains approximately the same independently of the diversity

type and/or weights configuration for the region of interest where $P > -130$ dB. Note that for $P < -130$ dB, the AER performance is extremely poor, close to 0.5, independently of the ξ choice, which is the reason of the optimum ξ divergence in such operation region.. Interestingly, the optimum ξ decreases following a power-law as P increases.

C. On the Performance Impact of NLOS Scattering Noise and Number of Transmitted Tones

Throughout the paper, we have ignored the multi-path interference (scattering) phenomenon by assuming geometric mm-wave channels. In practice, NLOS scattering may not be completely ignored, thus, herein, we illustrate its potential performance impact. Specifically, we consider a scattering phase noise $\bar{\varphi} \sim \mathcal{N}(0, \bar{\sigma})$ to be included as an additional addend to the right-side term in (17) in NLOS conditions. Fig. 7 illustrates the achievable optimum AER performance (Fig. 7a) and corresponding ξ (Fig. 7b) as a function of $\bar{\sigma}$. Observe that as $\bar{\sigma}$ increases, the optimum AER decreases, while its corresponding ξ increases since the NLOS hypothesis becomes noisier, thus, diverges more from the purely-geometric LOS hypothesis. The trends related to the relative performance among full-diversity with equal/optimized weights and limited-diversity schemes remain similar to those observed in Fig. 6.

On the other hand, note that throughout the paper we assumed the transmission of a single tone/carrier, however, our framework can be easily extended to the multi-tone/carrier scenario. Specifically, one just needs to stack the relevant decision metric for each tone/carrier transmission f (25) to form an enlarged relevant decision metric Δ_i of dimensions $6F \times 1$ for each i , where F is the number of tone/carriers that are transmitted for carrier phase measurements. Moreover, the diagonal weighting matrix \mathbf{W} has now $6F \times 6F$ elements, and can still be similarly designed as described in Section IV-C according to an EQU, MNV or NVP approach.

Fig. 8 shows the optimum AER performance as a function of the number of transmitted tones/carriers F . Observe that the schemes with limited polarization diversity, and that with full polarization diversity and EQU/MNV weighting, benefit little from the frequency diversity induced by the multi-tone transmissions. Meanwhile, the achievable AER under the full polarization diversity configuration with NVP weighting decreases exponentially with the number of transmitted signals.

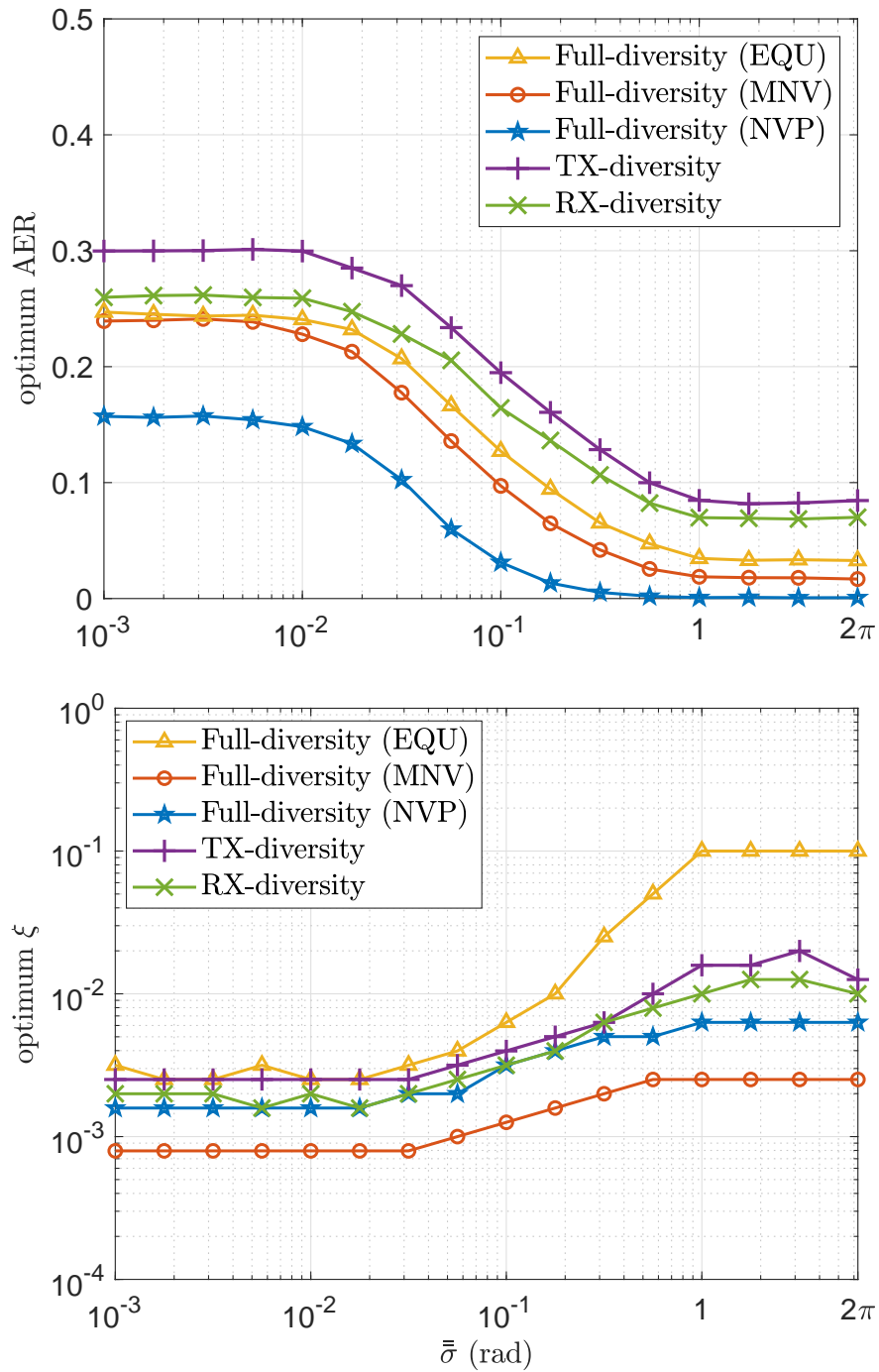


Fig. 7. a) Optimum AER (top), and b) corresponding ξ (bottom) as a function of the standard deviation of the scattering phase noise. We set $P = -100$ dB. In NLOS scenarios, the reflecting material is selected randomly among those given in Table I.

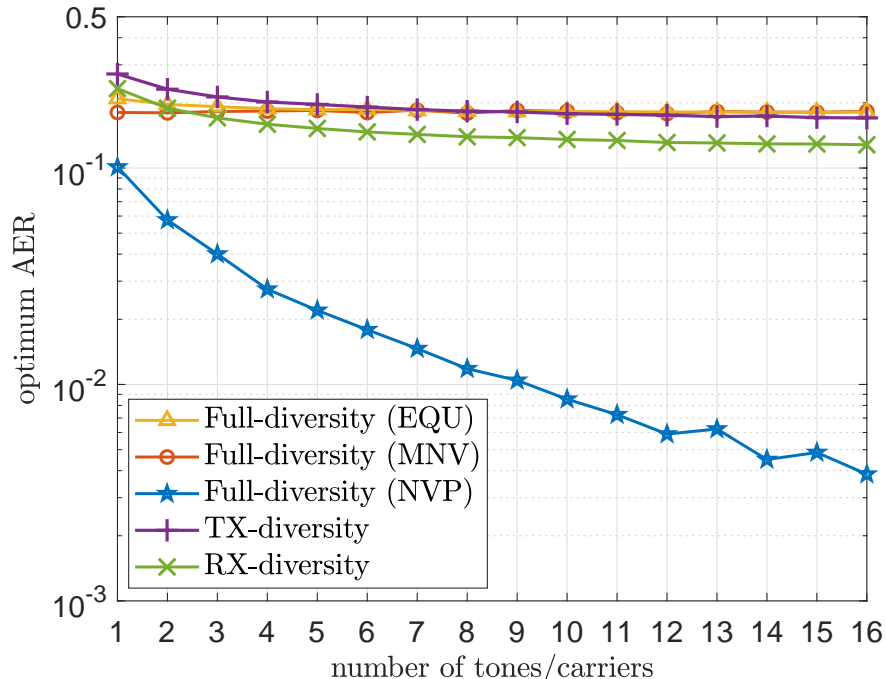


Fig. 8. Optimum AER as a function of the number of transmitted tones. We set $P = -100$ dB and $\bar{\sigma} = 3 \times 10^{-2}$ rad. Tones are spaced 1 MHz, and first tone is transmitted at 30 GHz. In NLOS scenarios, the reflecting material is selected randomly among those given in Table I.

VI. CONCLUSION

In this work, we proposed a threshold-based LOS/NLOS classifier exploiting weighted differential (over different polarization configurations) carrier phase measurements in a single mm-wave link. The proposed mechanism can work both in full and limited polarization diversity systems, and we developed a framework for assessing its performance. We conducted extensive simulations and showed that the performance of the proposed classifier, specified in terms of average error rate, depends critically on the potential reflecting materials in NLOS scenarios. For instance, the classifier is far more efficient in NLOS scenarios with wooden reflectors than in those with metallic reflectors. We illustrated the enormous performance gains that can be attained from exploiting full polarization diversity, properly weighting the differential carrier phase measurements, and using multi-signal/tone transmissions. Finally, we showed that the optimum decision threshold remains approximately the same independently of the material of potential NLOS reflectors, while it decreases following a power-law as the average path/link power gain increases.

REFERENCES

- [1] C. de Lima, D. Belot, R. Berkvens, A. Bourdoux, D. Dardari, M. Guillaud, M. Isomursu, E.-S. Lohan, Y. Miao, A. N. Barreto, M. R. K. Aziz, J. Saloranta, T. Sanguanpuak, H. Sardeddeen, G. Seco-Granados, J. Suutala, T. Svensson, M. Valkama, H. Wymeersch, and B. van Liempd (Eds.), “6G white paper on localization and sensing,” *6G Research Visions*, no. 12, 2020.
- [2] R. Di Taranto, S. Muppirisetty, R. Raulefs, D. Slock, T. Svensson, and H. Wymeersch, “Location-aware communications for 5G networks: How location information can improve scalability, latency, and robustness of 5G,” *IEEE Signal Processing Magazine*, vol. 31, no. 6, pp. 102–112, 2014.
- [3] E. S. Lohan, M. Koivisto, O. Galinina, S. Andreev, A. Tolli, G. Destino, M. Costa, K. Leppanen, Y. Koucheryavy, and M. Valkama, “Benefits of positioning-aided communication technology in high-frequency industrial IoT,” *IEEE Communications Magazine*, vol. 56, no. 12, pp. 142–148, 2018.
- [4] X. Hu, C. Zhong, Y. Zhang, X. Chen, and Z. Zhang, “Location information aided multiple intelligent reflecting surface systems,” *IEEE Transactions on Communications*, vol. 68, no. 12, pp. 7948–7962, 2020.
- [5] O. L. A. Lopez, N. H. Mahmood, H. Alves, C. M. Lima, and M. Latva-aho, “Ultra-low latency, low energy, and massiveness in the 6G era via efficient CSIT-limited scheme,” *IEEE Communications Magazine*, vol. 58, no. 11, pp. 56–61, 2020.
- [6] 3GPP TR 21.915, *Release 15 Description; Summary of Rel-15 Work Items*. [Online]. Available: <https://portal.3gpp.org/desktopmodules/Specifications/SpecificationDetails.aspx?specificationId=3389>
- [7] 3GPP TR 21.916, *Release 16 Description; Summary of Rel-16 Work Items*. [Online]. Available: <https://portal.3gpp.org/desktopmodules/Specifications/SpecificationDetails.aspx?specificationId=3493>
- [8] RP-210903, Intel Corp., CATT, Ericsson, *3GPP Work Item Description: Revised WID on NR Positioning Enhancements*. 3GPP TSG RAN Meeting #91e, March 2021.
- [9] 3GPP, “Study on NR positioning support,” 3GPP TR 38.855, Tech. Rep. 16, 2018.
- [10] Z. Lin, T. Lv, and P. T. Mathiopoulos, “3-D indoor positioning for millimeter-wave massive MIMO systems,” *IEEE Transactions on Communications*, vol. 66, no. 6, pp. 2472–2486, 2018.
- [11] S. Dwivedi, R. Shreevastav, F. Munier, J. Nygren, I. Siomina, Y. Lyazidi, D. Shrestha, G. Lindmark, P. Ernström, E. Stare *et al.*, “Positioning in 5G networks,” *arXiv preprint arXiv:2102.03361*, 2021.
- [12] C. De Lima, D. Belot, R. Berkvens, A. Bourdoux, D. Dardari, M. Guillaud, M. Isomursu, E.-S. Lohan, Y. Miao, A. N. Barreto, M. R. K. Aziz, J. Saloranta, T. Sanguanpuak, H. Sardeddeen, G. Seco-Granados, J. Suutala, T. Svensson, M. Valkama, B. Van Liempd, and H. Wymeersch, “Convergent communication, sensing and localization in 6G systems: An overview of technologies, opportunities and challenges,” *IEEE Access*, vol. 9, pp. 26 902–26 925, 2021.
- [13] Samsung, “System-level performance evaluation for RAT-dependent positioning techniques,” 3GPP TSG RAN WG1 Meeting RAN#96, Athens, Greece, Tech. Rep. R1-1902246, 2019.
- [14] Ericsson, “System level performance evaluation for RAT-dependent positioning techniques,” 3GPP TSG RAN WG1 Meeting RAN#96, Athens, Greece, Tech. Rep. R1-1903142, 2019.
- [15] Intel, “NR positioning evaluation results,” 3GPP TSG RAN WG1 Meeting RAN#96, Athens, Greece, Tech. Rep. R1-1902514, 2019.
- [16] F. H. Fraunhofer IIS, “Carrier phase enhanced potential solution for NR positioning schemes,” 3GPP TSG RAN WG1 Meeting RAN#96, Athens, Greece, Tech. Rep. R1-1903055, 2019.
- [17] CATT, “Discussion of NR positioning enhancements,” Meeting#102, Online, Tech. Rep. R1-2005712, 2020.
- [18] D. University, “Carrier phase based positioning for NR,” Meeting#104bis-e, Online, Tech. Rep. R1-2005712, 2021.

- [19] K. Witrisal, P. Meissner, E. Leitinger, Y. Shen, C. Gustafson, F. Tufvesson, K. Haneda, D. Dardari, A. F. Molisch, A. Conti, and M. Z. Win, "High-accuracy localization for assisted living: 5G systems will turn multipath channels from foe to friend," *IEEE Signal Processing Magazine*, vol. 33, no. 2, pp. 59–70, 2016.
- [20] H. Wymeersch, D. Shrestha, C. M. de Lima, V. Yajnanarayana, B. Richerzhagen, M. F. Keskin, K. Schindhelm, A. Ramirez, A. Wolfgang, M. F. de Guzman, K. Haneda, T. Svensson, R. Baldemair, and S. Parkvall, "Integration of communication and sensing in 6G: a joint industrial and academic perspective," in *IEEE 32nd Annual International Symposium on Personal, Indoor and Mobile Radio Communications (PIMRC)*, 2021, pp. 1–7.
- [21] J. Borras, P. Hatrack, and N. Mandayam, "Decision theoretic framework for NLOS identification," in *VTC'98. 48th IEEE Vehicular Technology Conference. Pathway to Global Wireless Revolution (Cat. No.98CH36151)*, vol. 2, 1998, pp. 1583–1587 vol.2.
- [22] B. J. Silva and G. P. Hancke, "Non-line-of-sight identification without channel statistics," in *IECON The 46th Annual Conference of the IEEE Industrial Electronics Society*, 2020, pp. 4489–4493.
- [23] Y. Zhu, T. Ma, Z. Li, D. Sun, X. Sun, X. Zhao, and F. Hu, "NLOS identification and correction based on multidimensional scaling and quasi-accurate detection," *IEEE Access*, vol. 7, pp. 53 977–53 987, 2019.
- [24] S. Sosnin, A. Lomayev, and A. Khoryaev, "NLOS links detection algorithm for improved 5G NR indoor positioning," in *IEEE International Black Sea Conference on Communications and Networking (BlackSeaCom)*, 2021, pp. 1–6.
- [25] Z. Xiao, H. Wen, A. Markham, N. Trigoni, P. Blunsom, and J. Frolik, "Non-line-of-sight identification and mitigation using received signal strength," *IEEE Transactions on Wireless Communications*, vol. 14, no. 3, pp. 1689–1702, 2015.
- [26] C. Wu, H. Hou, W. Wang, Q. Huang, and X. Gao, "TDOA based indoor positioning with NLOS identification by machine learning," in *10th International Conference on Wireless Communications and Signal Processing (WCSP)*, 2018, pp. 1–6.
- [27] Q. Liu, Z. Huang, and J. Wang, "Indoor non-line-of-sight and multipath detection using deep learning approach," *GPS Solutions*, vol. 23, no. 3, pp. 1–14, 2019.
- [28] K. Bregar and M. Mohorčič, "Improving indoor localization using convolutional neural networks on computationally restricted devices," *IEEE Access*, vol. 6, pp. 17 429–17 441, 2018.
- [29] J. Park, S. Nam, H. Choi, Y. Ko, and Y.-B. Ko, "Improving deep learning-based UWB LOS/NLOS identification with transfer learning: An empirical approach," *Electronics*, vol. 9, no. 10, p. 1714, 2020.
- [30] V. B. Vales, T. Domínguez-Bolaño, C. J. Escudero, and J. A. García-Naya, "Using the power delay profile to accelerate the training of neural network-based classifiers for the identification of LOS and NLOS UWB propagation conditions," *IEEE Access*, vol. 8, pp. 220 205–220 214, 2020.
- [31] J. Fan and A. S. Awan, "Non-line-of-sight identification based on unsupervised machine learning in ultra wideband systems," *IEEE Access*, vol. 7, pp. 32 464–32 471, 2019.
- [32] A. Kirmaz, D. S. Michalopoulos, I. Balan, and W. Gerstacker, "LOS/NLOS classification using scenario-dependent unsupervised machine learning," in *IEEE 32nd Annual International Symposium on Personal, Indoor and Mobile Radio Communications (PIMRC)*, 2021, pp. 1134–1140.
- [33] M. Giordani, M. Polese, A. Roy, D. Castor, and M. Zorzi, "A tutorial on beam management for 3GPP NR at mmWave frequencies," *IEEE Communications Surveys Tutorials*, vol. 21, no. 1, pp. 173–196, 2019.
- [34] J. Bang, H. Chung, J. Hong, H. Seo, J. Choi, and S. Kim, "Millimeter-wave communications: Recent developments and challenges of hardware and beam management algorithms," *IEEE Communications Magazine*, vol. 59, no. 8, pp. 86–92, 2021.
- [35] P. Zand, J. Romme, J. Govers, F. Pasveer, and G. Dolmans, "A high-accuracy phase-based ranging solution with Bluetooth Low Energy (BLE)," in *IEEE Wireless Communications and Networking Conference (WCNC)*, 2019, pp. 1–8.

- [36] Core Specification Working Group, "Bluetooth Core Specification v5.2," Dec. 2019. [Online]. Available: <https://www.bluetooth.com/specifications/bluetooth-core-specification/>
- [37] S. Jaeckel, K. Borner, L. Thiele, and V. Jungnickel, "A geometric polarization rotation model for the 3-D spatial channel model," *IEEE Transactions on Antennas and Propagation*, vol. 60, no. 12, pp. 5966–5977, 2012.
- [38] Y. Ma, B. Wang, S. Pei, Y. Zhang, S. Zhang, and J. Yu, "An indoor localization method based on AOA and PDOA using virtual stations in multipath and NLOS environments for passive UHF RFID," *IEEE Access*, vol. 6, pp. 31 772–31 782, 2018.
- [39] S. Grimnes and Ørjan G Martinsen, "Chapter 3 - dielectrics," in *Bioimpedance and Bioelectricity Basics (Third Edition)*, third edition ed., S. Grimnes and O. G. Martinsen, Eds. Oxford: Academic Press, 2015, pp. 37–75. [Online]. Available: <https://www.sciencedirect.com/science/article/pii/B9780124114708000039>
- [40] A. D. Rakić, A. B. Djurišić, J. M. Elazar, and M. L. Majewski, "Optical properties of metallic films for vertical-cavity optoelectronic devices," *Applied optics*, vol. 37, no. 22, pp. 5271–5283, 1998.
- [41] S. Alekseev and M. Ziskin, "Reflection and absorption of millimeter waves by thin absorbing films," *Bioelectromagnetics: Journal of the Bioelectromagnetics Society, The Society for Physical Regulation in Biology and Medicine, The European Bioelectromagnetics Association*, vol. 21, no. 4, pp. 264–271, 2000.
- [42] Y. Wu, M. Han, T. Liu, and L. Deng, "Studies on the microwave permittivity and electromagnetic wave absorption properties of Fe-based nano-composite flakes in different sizes," *Journal of Applied Physics*, vol. 118, no. 2, p. 023902, 2015.
- [43] P. Henkel, "Reliable carrier phase positioning," Ph.D. dissertation, Technische Universität München, 2010.
- [44] C. A. Balanis, *Antenna theory: analysis and design*. John wiley & sons, 2015.